

You may also like

The Giotto three-dimensional positive ion analyser

To cite this article: A D Johnstone *et al* 1987 *J. Phys. E: Sci. Instrum.* **20** 795

View the [article online](#) for updates and enhancements.

- [Measurement technique for the Giotto radio science experiment](#)
P Edenhofer, M K Bird, H Buschert et al.
- [A comprehensive model for quantum noise characterization in digital mammography](#)
P Monnin, H Bosmans, F R Verdun et al.
- [COMET 1P/HALLEY MULTIFLUID MHD MODEL FOR THE GIOTTO FLY-BY](#)
M. Rubin, M. R. Combi, L. K. S. Daldorff et al.

The Giotto three-dimensional positive ion analyser

A D Johnstone[†], A J Coates[†], B Wilken[‡], W Studemann[‡],
W Weiß[‡], R Cerulli Irelli[§], V Formisano[§], H Borg^{||}, S Olsen^{||},
J D Winningham[¶], D A Bryant^{*} and S J Kellock^{†+}

[†] Mullard Space Science Laboratory, Holmbury St Mary, UK

[‡] Max-Planck-Institut für Aeronomie, Katlenburg-Lindau,
Federal Republic of Germany

[§] Istituto di Fisica dello Spazio Interplanetario, Frascati, Italy

^{||} Kiruna Geophysical Institute, Kiruna, Sweden

[¶] Southwest Research Institute, San Antonio, Texas, USA

^{*} Rutherford Appleton Laboratory, Chilton, Didcot,
Oxfordshire, UK

Received 11 March 1987

Abstract. The three-dimensional velocity distribution of positive ions in the neighbourhood of comet Halley was measured by an instrument which included two complementary sensors. The fast ion sensor measured the energy/charge distribution from 10 eV/q to 20 keV/q once per revolution of the spacecraft. It obtained the characteristics of the solar wind flow near the comet. The implanted ion sensor measured the energy/charge distribution from 90 eV/q to 90 keV/q with discrimination into five mass groups in a period of 32 spacecraft revolutions. These observations provided the angular distribution of the cometary ions formed by the ionisation of gas molecules sublimed from the cometary nucleus. In this paper the relation between the raw count rates and the plasma parameters for the fast ion sensor is derived on the basis of a complete energy angle scan of the sensor in a calibration source. The accuracy of the analysis was tested by two techniques using data collected during the mission. One required a special operation of the spacecraft; the other involved a comparison with magnetic field measurements. Both lead to the conclusion that velocity components of the order of a few km s⁻¹ perpendicular to the main flow velocity of the order of 400 km s⁻¹ can be accurately recorded.

1. Introduction

It has been known for some time (Biermann 1951) that the plasma tail of a comet is the visible manifestation of the interaction between plasma from two distinct sources: ionised particles of cometary origin and the solar wind. Theoretical analyses of this interaction (Biermann *et al* 1967, Wallis 1973, Ip and Axford 1982) provided a model of the gross features of the plasma flow to be expected near the comet, but they did not give a detailed explanation of the formation of the visible tail. On the other hand, many of the features predicted by theory could not be observed from the Earth, because they produce no visible effects. The gap between theoretical analysis of the solar wind/comet interaction and ground-based observations of comet tails could only be filled by *in situ* measurements of the plasma distributions within the coma of a comet. It was the task for the plasma instruments on Giotto to make these measurements and to fill this gap. Theory says that the plasma should be divided into three main regimes separated by two surfaces—a contact

surface and a bow shock. The contact surface encloses the region dominated by the cold, dense cometary plasma around the nucleus and separates it from the solar wind. The neutral cometary particles are not bound by this contact surface and may travel well upstream into the solar wind before being ionised. The additional mass they then add to the solar wind flow slows it down and eventually creates the second surface, a bow shock.

The objectives of the Johnstone plasma analyser (JPA) instrument were:

(a) to look for the existence of a bow shock and a contact surface;

(b) to observe the mass loading of the solar wind and the resultant deceleration and deflection of the flow;

(c) to observe the distribution of implanted cometary ions and its stability;

(d) to detect the principal ionisation mechanisms.

The instrument was designed to achieve these objectives by measuring the three-dimensional velocity distribution of positive ions in the energy range from 10 eV to 90 keV. It included two complementary sensors: the fast ion sensor (FIS) measured the energy per charge distribution from 10 eV/q to 20 keV/q in all directions, except for a cone around the velocity vector, once every rotation (nominally 4 s) of the spacecraft; the implanted ion sensor (IIS) measured the energy per charge distribution from 90 eV/q to 90 keV/q over a similar angular range, with discrimination into five mass groups, but took 32 rotations to obtain a complete distribution.

On an exploratory mission it is most important that the instruments are able to cope with a wide range of possible circumstances and that they are not limited by preconceived ideas of what the distributions might be like near a comet. They must cover as much of velocity space as possible, leaving no gaps in coverage for unsuspected distributions to slip through. This requirement has implications for the optics of the analyser design, as well as for the energy sweep rates and sampling patterns.

The JPA instrument was one of a group of complementary plasma sensors measuring ions on Giotto; the others were the IMS instrument (Balsiger *et al* 1986), the PICCA sensor of the RPA (Rème *et al* 1986) and the EPA instrument (McKenna-Lawlor *et al* 1986). The JPA instrument was directed towards studies on the nature of the solar wind interaction with the comet rather than the detailed chemical composition of the ions.

The instrument consisted of three separate packages: the fast ion sensor, the implanted ion sensor and the data processing unit (figure 1).

The purpose of the FIS was to provide a three-dimensional distribution over the energy range likely to include most of the ions near the comet as quickly as possible. It obtained the full azimuthal distribution once per rotation of the spacecraft. It measured the solar wind distribution at its most anisotropic, giving the flow speed and direction, temperature and density. It followed the development of the solar plasma as it was thermalised, slowed down and deflected. It measured the distributions of the low-mass ions once the angle between the flow direction and magnetic field direction became small near the comet. Speed of response was achieved at the expense of mass discrimination, and by limiting the energy range from 10 eV to 20 keV. Its geometric factor was determined by ensuring that the count rate in the most anisotropic and dense solar wind to be expected would not exceed the highest allowable count rate. Its wide dynamic range then ensured that weak secondary populations could also be detected, with the highest possible statistical significance.

However, the mass distribution as well as the complete angular distribution of the implanted cometary ions must be

+ Present address: European Space Operations Centre, Darmstadt, Federal Republic of Germany.

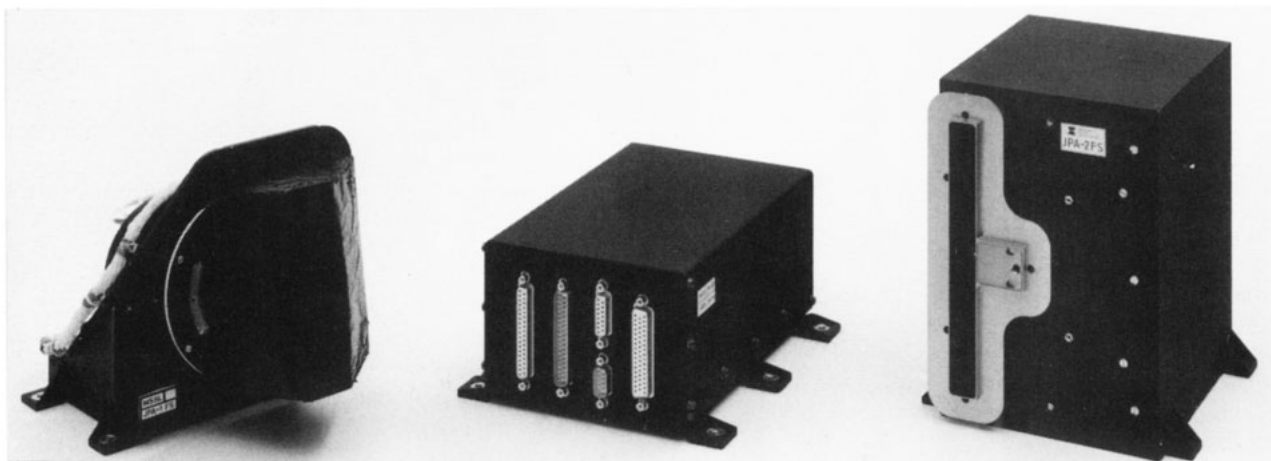


Figure 1. The flight units of the JPA instrument. From the left they are the fast ion sensor, the data processing unit and the implanted ion sensor. The units are approximately four times the size shown.

measured if the characteristics of the flow are to be understood because the behaviour is strongly species-dependent, although it is not necessary to have the same mass resolution as for studies of the chemical constituents of the nucleus. The task for the IIS, therefore, was to search for massive cometary ions in the solar wind by extending the energy range of the measurements up to 90 keV, increasing the sensitivity so that very low densities could be measured and providing mass discrimination sufficient to separate the ions into the principal mass groups. The technique used to obtain the mass discrimination, namely time-of-flight analysis, had the additional property of having a very low background because it used a coincidence technique. This meant that extremely low count rates could be measured with long enough integration times. It achieved these properties at the expense of speed of response because it measured at one energy level each rotation of the spacecraft. With its high sensitivity, it was unable to measure the proton flux in the solar wind because the intense fluxes overloaded the time-of-flight analysers.

The data processing unit (DPU) collected the data from the sensors and processed it for transmission to Earth.

Neither of the sensors covered the distribution of cold cometary ions near the contact surface, which appeared to be moving antiparallel to the spacecraft velocity vector. There were several reasons for not covering this latter population. First, the fluxes were very much higher than any other fluxes encountered and if the sensitivity of the FIS had been reduced to cope with the cometary ions it would not have adequate sensitivity for other important populations. Secondly, to detect these ions would have meant exposing the sensor to the flux of cometary dust and neutral particles past the spacecraft, which would have created an undesirable background in the sensor for all of the measurements.

In this paper the fast ion sensor and the approach used to analyse its data is described in detail. The implanted ion sensor is described briefly here and in more detail in a companion paper (Wilken *et al* 1987).

2. The fast ion sensor

The principal design aims of this sensor were:

- (a) high sensitivity, i.e. a large geometric factor;
- (b) wide dynamic range, i.e. high maximum count rates and low background;
- (c) complete and continuous coverage of a wide solid angle, in the energy range from 10 eV to 20 keV for positive ions;
- (d) angular and energy resolution good enough to resolve the supersonic flow in the solar wind.

The coverage in solid angle was achieved by having a wide angle of acceptance (150°) for the analyser in a plane containing the spin axis of the spacecraft. Then, as the spacecraft rotated, the detectors swept through 96% of the full 4π solid angle omitting only a 20° cone around the velocity vector and a 10° cone around the opposite direction.

The fast ion sensor (FIS) consisted of four principal elements (figure 2): a hemispherical electrostatic energy analyser, a quadrispherical angular dispersion sector, a microchannel plate detector and a discrete-anode, position-sensitive read-out system (Johnstone *et al* 1985).

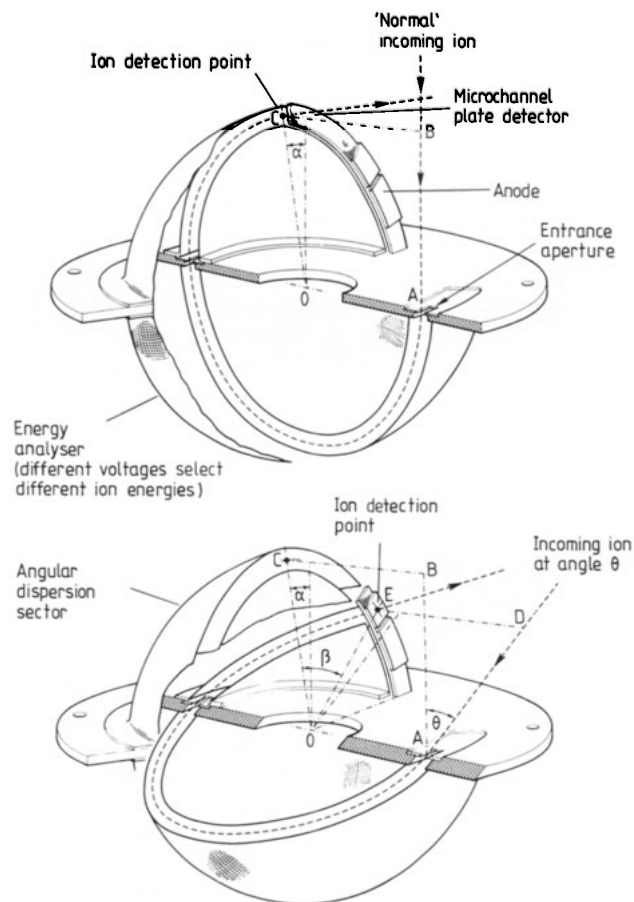


Figure 2. Diagram showing the principle of operation of the fast ion sensor.

Table 1. FIS polar angles[†] sampled by the accumulators.

	Angles sampled in wide-energy mode	[GF] ($\times 10^{10} \text{ m}^2 \text{ sr}$)	Angles sample in solar wind mode	[GF] ($\times 10^{10} \text{ m}^2 \text{ sr}$)
1	98–124	20.4	98–150	41.1
2	124–150	20.6	46–98	58.3
3	46–72	31.6	46–59	15.5
4	72–98	26.7	59–72	16.1
5	20–46	9.2	72–85	14.1
6	150–180	11.7	85–98	12.6

[†] Measured from comet–spacecraft relative velocity vector.

After entering the aperture, ions passed through a hemispherical energy analyser, which selected a narrow band in energy per charge ($\delta E/E = 4.7\%$). After an intermediate aperture, the selected ions entered an 80° angular dispersion sector, which dispersed them to emerge around a 150° annular sector according to the angle of incidence at the input aperture. They were then accelerated onto the front face of a microchannel plate detector, which produced a cloud of electrons for each ion striking the input. Finally, the electrons were collected on one of a series of eight metal anodes behind the microchannel plate. Each of the anodes covered a defined angular range (table 1) and was connected to a charge-sensitive pulse amplifier mounted within the sensor which produced a logic level pulse output for each electron cloud striking the anode. The arrangement provided continuous coverage over the sensor field of view.

The energy of the detected ion was known from the analysis voltage applied to the spherical deflection plates. The plate voltages are applied in a fixed ratio $V_{\text{(inner)}}/V_{\text{(outer)}} = -1.18$, to give the zero-potential surface exactly halfway between the spherical plates. The ‘gain’ of the analyser (i.e. the ratio of the energy selected to the plate potential difference) is 3.55. The polar angle was known from the anode which registered the count. The azimuthal angle was measured by timing with respect to the spacecraft Sun pulse.

The detector consisted of two double-thickness micro-channel plates in a chevron configuration, specially cut to cover the 150° arc of the output aperture of the analyser. The combination produced a saturated pulse distribution, with a full width at half maximum of 70% at a gain of 2×10^6 . The saturated distribution enabled reliable operation in a pulse counting mode, with little dependence of the overall detection efficiency on the amplifier gain or threshold. Achieving the saturation at a low gain enabled the plate to operate at high count rates and thus maximised the dynamic range. The maximum pulse rate the channel plate can deliver per anode sector is of the order of 2×10^6 pulses/s. In principle, such count rates could have been coped with if they had occurred simultaneously in all sectors.

The energy passband of the analyser was swept continuously, along an exponential decay curve from the maximum energy of 20 keV down to 10 eV in one sixteenth of a spin. The sweep was synchronised to the spin by using the spacecraft spin segment clock pulse to control the sweep. Since the angle of acceptance in the spin plane is 5° , there were gaps in the azimuthal coverage between successive sweeps which were 22.5° apart. This is important in the solar wind where the undisturbed solar wind may be confined within an angular range of 5° . In order to provide contiguous azimuthal coverage, an energy sweep covering one quarter of the energy range (a factor of 6.7 in energy) was used four times as often in the 45° angular

sector centred on the solar direction. This solar wind mode was used on alternate spins, giving a time resolution for solar wind measurements of 8 s.

The range of 6.7 is not enough to cover the solar wind under all conditions. For example, during the cruise phase the solar wind speed varied between 350 km s^{-1} , an energy of 650 eV, and 900 km s^{-1} , an energy of 4000 eV. The instrument was therefore designed so that the starting point of the solar wind sweep could be set in eight positions (table 2) within the overall range.

Table 2. Start and stop energy levels for FIS solar wind sweeps.

Solar wind sweep preset	Start energy (eV/q)	Proton velocity (km s^{-1})	Stop energy (eV/q)	Proton velocity (km s^{-1})
7	19963	1962	4161	895
6	15956	1754	2494	693
5	9562	1358	1494	536
4	5730	1051	896	415
3	3434	813	537	321
2	2058	630	322	249
1	1233	487	193	192
0	739	377	115	149

It was realised that as the spacecraft approached the comet the solar wind would slow down in a way that could not be anticipated. Since the round-trip light time during the encounter was 16 min, it would be impossible to respond quickly enough to such changes by ground command. Therefore an autoranging function, operating in software, was included in the DPU. After collecting the data for one sample in the solar wind mode, the DPU scanned through the spectrum it had just collected for the energy channel with the peak count. If the energy level of the peak count did not lie within a range of eight levels, then the start of the next sweep was changed up or down accordingly by one quarter of the range of the sweep. Since the peak count is the peak of the proton spectrum, its position was kept in the third quarter from the top of the energy sweep. This ensured that the alpha particle distribution, which appears at twice the energy of the proton distribution, but at a much lower intensity, was also covered. One possible failure of such a mode would be for the instrument to latch on to a lesser peak and follow it, thereby missing the main part of the solar wind. To avoid this problem two further functions were included. First of all the DPU conducted a significance test on the peak. If there were fewer than 64 counts at the peak, then the energy was switched to the

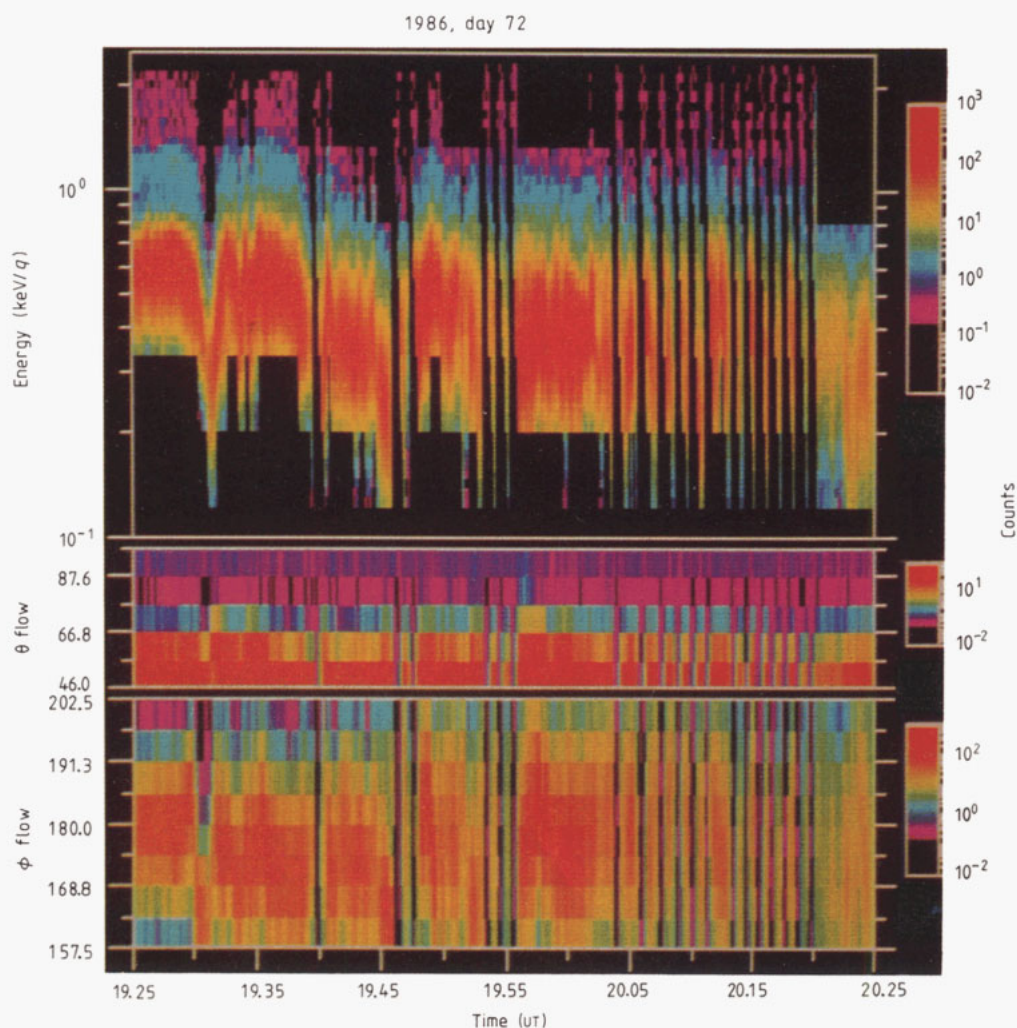


Figure 3. A colour spectrogram of the FIS data from the crossing of the bow shock of comet Halley. The top panel shows the data summed over all angles as a function of energy. Similarly the middle panel shows the data summed over energy and azimuthal angle, and the bottom panel shows the data summed over energy and polar angle.

next lower range. If it had failed to find a significant peak by the time it reached the lowest level, then it would switch to the highest level and continue to cycle down. Finally, if neither of these programs was satisfactory, the autoranging program could be disabled and the start level set to any desired position by ground command.

All three possibilities were demonstrated during the crossing of the bow shock of comet Halley as shown in figure 3. As the bow shock was approached, the spacecraft encountered at 19.31 GRT (ground received time in UT) a sudden large decrease in the solar wind velocity from 295 to 190 km s⁻¹. In order to follow this extremely interesting phenomenon, the autoranging program had to change the preset level from 2 to 1 to 0 and then back again over a period of 4 min. It is evident from figure 3 that without the autoranging facility this event would not have been covered properly. Eventually, as the solar wind distribution broadened, the peak count dropped and the autoranging started to cycle through the complete range.

This is visible in the data as vertical black bands through the solar wind. At 20.00 UT the experiment control team at the European Space Operations Centre in Darmstadt, FR Germany initiated a command to switch off the autoranging and set it at the lowest level. The command was executed at 20.20 GRT. The characteristics of the fast ion sensor are listed in table 3.

3. The implanted ion sensor

The implanted ion sensor (IIS) is an ion spectrometer (figure 4)

Table 3. FIS characteristics.

E/q range (keV/ q)	0.01–20
Acceptance angles	
azimuthal	5°
polar	160°
Outer plate radius r_1 (mm)	38
Inner plate radius r_2 (mm)	33
Centre radius r (mm ²)	35.5
Analyser gain ($= r/2(r_1 - r_2)$)	3.55
Aperture diameter (mm)	2.25
Aperture area (mm ²)	4
Plate voltage splitting (V_2/V_1)	– 1.18
Energy resolution ($\delta E/E$)	4.7%
Geometric factor (mm ² sr eV)	$4.7 \times 10^{-3} E(\text{eV})$
(26° anode at normal incidence)	

which combines electrostatic analysis with a time-of-flight measurement. An electrostatic analyser selects positive ions of a given energy per charge, E/q . The ions are then accelerated by a potential difference V before the time T to travel a path length D is determined. The measured quantities E/q and the time-of-flight T can be combined to yield the mass-to-charge ratio M/q according to the equation

$$M/q = 2WT^2/qD^2$$

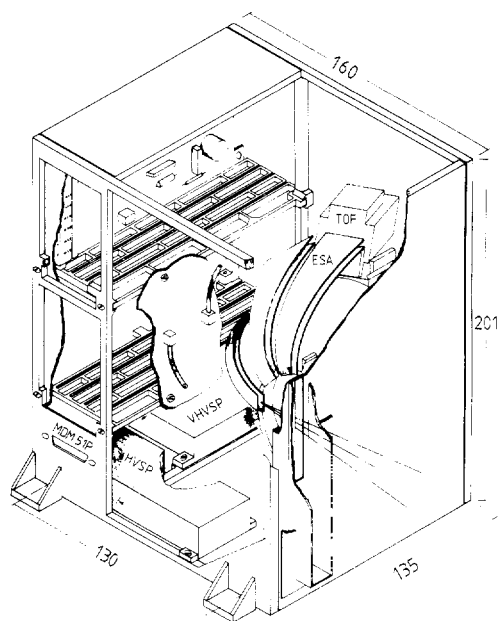


Figure 4. A perspective, cut-away view of the implanted ion sensor showing part of the array of electrostatic analysers (ESA) and time-of-flight analyser (TOF). The high-voltage supplies VHVSP and HVSP are mounted in the base beneath the electronic cards.

where W , the total energy after post-acceleration, is given by

$$W = q(V + E/q).$$

The instrument contains five sensors, each consisting of a spherical-section electrostatic energy analyser and a time-of-flight (TOF) analyser (figure 4). The five sensors are arranged as an angular array to cover the range 15° to 165° , in five equally spaced sectors 10° wide relative to the spin axis of the spacecraft. As the spacecraft rotates, the angular distribution of the ions is obtained as with the FIS.

As the ions leave the electrostatic analyser (figure 4), they are accelerated by 10 kV before striking a thin ($0.05 \mu\text{g mm}^{-2}$), grid-supported carbon foil at the entrance to the time-of-flight analyser.

Ions passing through the carbon foil transfer a small fraction of their energy to secondary electrons. Those secondaries that escape from the foil are accelerated by 0.7 kV and deflected towards the microchannel plates. The fast output pulses of the microchannel plate (typical risetime of ~ 0.9 ns) result in an accurate timing pulse for the START signal. Essentially the same principle is used in the STOP detector, except that the secondary electrons are generated in the surface layer of an aluminium absorber. Although the ions enter the time-of-flight system on approximately parallel trajectories, Coulomb interaction with the atoms in the carbon foil results in strong angular scattering. The variations in the flight path are limited to $\pm 5\%$ by using a spherical concave converter surface for the STOP detector.

The time required to process the signals from a single event is $25 \mu\text{s}$. Within this processing period, further START pulses and valid START–STOP combinations are recorded but cannot be processed.

Two separate count rates are monitored: the number of START pulses and the number of valid START–STOP combinations (TAC pulses). The requirement of a valid START–STOP combination gives a high rejection of background signals from penetrating radiation and detector noise and enables very low counting rates to be reliably measured.

Monitoring the number of START pulses enables the amount of deadtime in the instrument to be estimated. For example, it cannot record accurately (and was not intended to do so) the high flux of protons in the solar wind. The START count indicates the number of events that could not be processed.

Three types of distribution are telemetered from the sensor. The 256 level TOF spectrum is integrated over all angles for each spin; the four-dimensional distribution comprising five mass groups, five polar angle zones, eight or 16 azimuthal sectors and 32 energy levels, and the START and TAC totals in 16 sectors each spin. The complete distribution requires 32 spins or approximately 128 s to accumulate. The detector characteristics are summarised in table 4.

Table 4. IIS characteristics.

E/q range (keV/q)	0.090–90
Acceptance angles (each sensor)	
azimuthal	6°
polar	10°
Outer plate radius (mm)	51.5
Inner plate radius (mm)	48.5
Analyser gain	8.3
Plate voltage splitting	
inner	–11V to –11 kV
outer	0
Aperture area (mm^2)	42
Energy resolution ($\delta E/E$)	10%
Time-of-flight path length (mm)	22
Geometric factor ($\text{mm}^2 \text{ sr eV}$)	$7.6 \times 10^{-2} E(\text{eV})$

4. Onboard data processing

The measurement sequence of the instrument was synchronised to the spacecraft rotation. Two standard signals from the spacecraft were used to achieve the synchronisation: the Sun reference pulse (SRP) and the spin segment clock pulse (SSCP). The latter divided the period between successive SRPs by 16 384. The FIS sequence had a duration of two spins beginning 22.5° before the sensor's field-of-view fan crossed the solar direction. Each spin was divided into eight sectors of 45° . During the first sector the sensor operated in the solar wind mode, making eight short energy sweeps. In the remaining seven sectors of the first spin, and for all eight sectors of the second spin, the sensor operated in the wide-energy mode, making two full energy sweeps in each sector. The IIS sequence had a duration of 32 spins, holding each of its energy levels for one complete spin. All the measurements were synchronised to the rotation, so that each value received at the ground was already associated with its direction without needing reference to the spacecraft attitude solution.

The data were acquired from the sensors each spin in the form of an array of up to third order, i.e. counts [energy (or mass), polar angle, azimuthal angle]. The array was produced with the intrinsic resolution of the sensor. For the FIS in wide-angle mode, this was 30 energies, six polar angle zones (the detector anodes) and 16 azimuthal sectors (corresponding to energy sweeps). The size of this array was greater than could be accommodated by the telemetry allocation and so the array was compressed by combining adjacent elements. This was done in more than one way for a particular array so that different aspects of the data were covered. The transmitted arrays are listed in tables 5 and 6.

A second level of data compression was carried out on the

Table 5. FIS transmitted distributions.

	Polar ^a zones (deg)	Azimuthal resolution (deg)	Energy spectrum	Time resolution	Mass information	When used
Wide-energy mode	20–72	45	15 contiguous bands	One spin	None	All
FTR ^b distribution	72–124	45				
	124–180	45	$\delta E/E = 0.6$ 10 eV to 20 keV			
Wide-energy mode	20–46	45	30 contiguous bands	Three spins	None	Format 1
HAR ^c distribution	46–72	45				
	72–98	22.5	$\delta E/E = 0.3$			
	98–124	22.5	10 eV to 20 keV			
	124–150	45				
	150–180	45				
Solar wind mode	46–98	5.6	30 contiguous bands	Two spins	None	Format 1 Format 3
SWA ^d distribution			$\delta E/E = 0.096$ E^* to $6.7 E^*$			
Solar wind mode	46–59	45	30 contiguous bands	Two spins	None	Format 1 Format 3
SWP ^e distribution	59–72	45				
	72–85	45	$\delta E/E = 0.096$			
	85–98	45	E^* to $6.7 E^*$			
	98–150	45	E^* set by command or onboard processing			

^a Measured from z axis.^b FTR, fast time resolution.^c HAR, high angular resolution.^d SWA, solar wind azimuthal.^e SWP, solar wind polar.

numbers themselves. The accumulation was carried out in 16 bit registers which the DPU compressed to 8 bits in a quasi-logarithmic way. The first four bits, effectively the exponent, denoted the position of the first non-zero bit in the number, and the remaining four transmitted bits contained the next four bits of the original number, the mantissa. The maximum error from the truncation was therefore 3.1%. This scheme is capable of compressing from 19 bits to 8 bits so there are some exponents (the hexadecimal values D , E and F) which do not occur in real data and can be used for other purposes.

Since the instrument was spin-synchronised, it produced a fixed number of data words each rotation. The spin period can vary with respect to the telemetry format duration, so that there had to be a means of allowing for a variation in the number of words transmitted. This was achieved by devising an instrument telemetry format that was spin-synchronised and had a basic length corresponding to a rotation of 45° . This JPA format ‘floated’ within the spacecraft telemetry format and was identified by three format sync. words. These words began with the three hexadecimal numbers not obtained from the data compression, i.e. D , E and F . The second half of each sync. word contained further information about the sequence and the instrument status. The telemetry output was double-buffered. In one side, a table of values was compiled from the data currently being acquired, while values acquired during the previous sector were read out to the telemetry from the other side. If the table of values had not been completely read out by the telemetry by the

end of a 45° sector, then the remaining values were lost when the buffers were interchanged. The order in which the data were compiled in the table was prioritised. Each type of distribution, e.g. 4DF or FTR (see tables 5 and 6), was transmitted completely before the next was started. Where a distribution might have been only partially transmitted, the order in which the values were listed was also designed to minimise the loss of information. For example, alternative energy levels through the spectrum were transmitted first and then the intermediate values were sent. This ensured that a coarse spectrum over the full range was transmitted first.

5. Theory of measurements and data analysis

5.1. Relation between count rate and phase space density

The scientific analysis will be undertaken at several levels of processing. Some features are apparent even in raw telemetry data as a discontinuity. Studies of the mass loading of the flow and the structure of the bow shock require the derivation of such bulk plasma parameters as density, temperature, velocity, pressure and possibly higher-order terms. To understand the stability of the cometary ions requires detailed analysis of the complete distribution function. The raw data from the instruments consist of the number of counts N registered on an anode in a fixed period of time dt . In order to make use of the information in anything more than a qualitative fashion, this number must be converted into a value which gives the density

Table 6. IIS transmitted distributions.

	Polar ^a zones (deg)	Azimuthal resolution (deg)	Energy spectrum	Time resolution	Mass information	When used
4DF ^b distribution	15–25	22.5	32 levels	32 spins	5 mass	Format 1
	50–60	22.5	$\delta E/E = 0.1$		groups	
	85–95	22.5	90 eV to 90 keV		1	
	120–130	22.5			2–11	
	155–165				12–22	
4DH ^c distribution	15–25	45	32 levels	32 spins	5 mass	Format 2 Format 3
	50–60	45	$\delta E/E = 0.1$		groups	
	85–95	45	90 eV to 90 keV		1	
	120–130	45			2–11	
	155–165				12–22	
TOF ^d distribution	15–165	360	32 levels	32 spins	256	Format 1
	(all polar zones combined)		$\delta E/E = 0.1$		time-of-flight	
			90 eV to 90 keV		groups	
START ^e	15–165	22.5	32 levels	32 spins	None	All
TAC ^f	15–165	22.5	32 levels	32 spins	None	All

^a Measured from z axis.^b 4DF, four-dimensional full resolution.^c 4DH, four-dimensional half resolution.^d TOF, time-of-flight spectrum.^e START, start pulse rate.^f TAC, timing processed pulses.

of particles in an elemental volume $d\mathbf{p} d\mathbf{q}$ of phase space, i.e.

$$N/G(\mathbf{p}) dt = f(\mathbf{p}, \mathbf{q}) d\mathbf{p} d\mathbf{q}$$

where \mathbf{q} is a position vector, \mathbf{p} the conjugate momentum and $G(\mathbf{p})$ is a detector function. In practice the explicit dependence on the spatial coordinates is ignored and, since the velocities are non-relativistic, velocity is used instead of momentum.

Over one spin the instrument scans velocity space, obtaining a matrix of values of $f_{ijk}(\mathbf{v})$. In this section we first describe the technique used to derive values of $f_{ijk}(\mathbf{v})$ from N using the sensor calibration, and then the way to obtain the bulk parameters from a summation over the matrix $f_{ijk}(\mathbf{v})$.

The counts in an accumulation bin of the sensor are

$$N = \int \mathbf{v} \cdot \mathbf{A} f(\mathbf{v}) G(\mathbf{v}) d\mathbf{v} dt \quad (1)$$

where \mathbf{A} is a vector whose magnitude is the aperture area and whose direction is along the normal. The integration is carried out over the volume of the accumulation bin. The function $G(\mathbf{v})$ is the detector response which is essentially defined by the equation (1). It has the property, like all electrostatic analysers, that

$$G(\mathbf{v}) = G(\mathbf{v}/v_0) = G(\mathbf{v}')$$

where v_0 is the centre velocity in the passband, i.e. the relative

shape stays the same when the centre velocity is changed. Then

$$\mathbf{v} \cdot \mathbf{A} G(\mathbf{v}) d\mathbf{v} = v_0^4 [\mathbf{v}' \cdot \mathbf{A} G(\mathbf{v}') v'^2 dv' d\Omega].$$

The quantity $[GF]$, the geometric factor,

$$[GF] = \int \mathbf{v}' \cdot \mathbf{A} G(\mathbf{v}') v'^2 dv' d\Omega \quad (2)$$

is a geometric property of the analyser which is independent of v_0 , the centre velocity, and can be obtained from the calibration.

When an unknown distribution is measured, we have to make the assumption that $f(\mathbf{v})$ is constant over the whole of the detector response, i.e. we assume that the region over which $G(\mathbf{v})$ is non-zero is small compared with the characteristic range over which the distribution function varies. It is the assumption that the sensor has been well designed for the task.

Then we can write

$$f(v_0) = N/(v_0^4 [GF] dt). \quad (3)$$

5.2. Obtaining the geometric factor from calibration

In the calibration, an ion beam was fired into the analyser at a series of angles and energies such that there were approximately 10 points within the passband in each energy or angle scan. The energy and angular spread of the beam was small compared with the width of the response function. Then the number of

counts in a calibration measurement was

$$N_b = T v_0 (\mathbf{v}_b' \cdot \mathbf{A}) G(\mathbf{v}_b') \int f_b(\phi) d\phi.$$

Here we have taken the distribution function of the calibration beam to be like a delta function in velocity space, i.e. $\delta(\mathbf{v} - \mathbf{v}_b)$, and the integral over time has been replaced by T , the accumulation time. The density of the beam is obtained by measuring the beam current with a Faraday cup whose collecting area is A_F , i.e.

$$\int f_b(\mathbf{v}) d\mathbf{v} = I_b / e v_b A_F$$

and $I_b = I_0 / S_b$ where I_0 is a standard current and S_b a weighting factor obtained from a regular series of measurements of the beam current. Each measurement gives a value

$$(\mathbf{v}_b' \cdot \mathbf{A}) G(\mathbf{v}_b') = e v_b A_F N_b S_b / I_0 T v_0.$$

The geometric factor, defined by equation (2), can be obtained from a summation over a series of calibration measurements:

$$[GF] = (e A_F / I_0 T) (v_b / v_0) \sum_b N_b S_b v'^2 \Delta v' (\sin \theta) \Delta \theta \Delta \phi.$$

The velocity space volume element is determined from the spacing of the measurement points. By making the $\Delta v'$ and $\Delta \theta$ steps constant, and by making the steps in ϕ inversely proportional to $\sin \theta$, i.e. putting $\Delta \phi = \Delta \phi' / \sin \theta = \text{constant}$, the volume element becomes a constant factor in the summation. Furthermore, since the velocity passband of the analyser is very narrow, $\Delta v / v \sim 0.05$, we can approximate

$$v_b / v_0 = 1 \quad v' = 1.$$

Then

$$[GF] = (e A_F \Delta v' \Delta \theta \Delta \phi' / I_0 T) \sum_b N_b S_b \quad (4)$$

where the summation is taken over the complete series of measurements covering the response of the analyser. A summation of the type in equation (4) is carried out for each anode of the detector, so that the geometric factor is finally specified by an array of values as in table 1.

The FIS was calibrated at Southwest Research Institute (Johnstone et al 1985). In all approximately 60 000 individual data points were collected per run in (energy, angle) space.

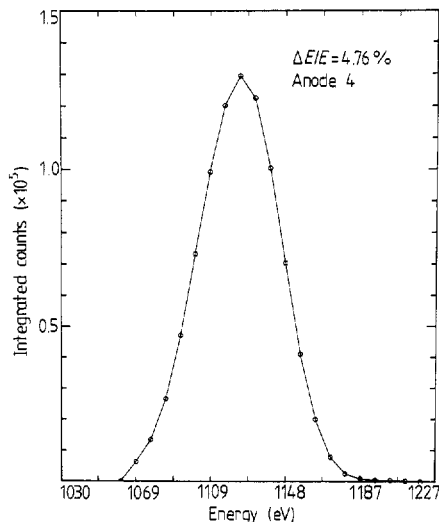


Figure 5. The energy response of one of the FIS anodes integrated over all angles of incidence.

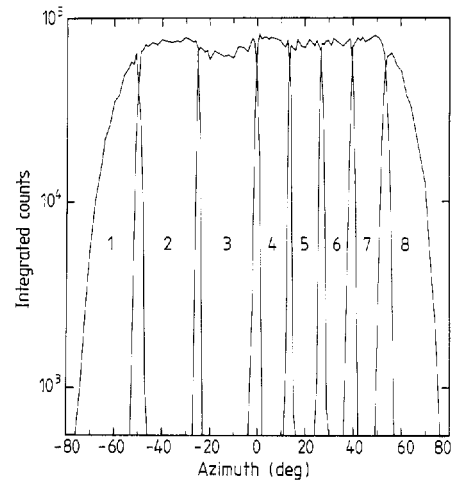


Figure 6. The geometric factor of each anode of FIS (numbered 1 to 8) as a function of the azimuth around the detector plane (corresponding to polar angle relative to the spin axis, with an offset of -80° when mounted in the spacecraft).

covering the complete angular and energy response of the analyser. The individual measurements were integrated to give the overall response of the sensor. The results are shown in figures 5 and 6. Although the aim was to achieve a polar angle coverage of 160° , the response falls off at large angles of incidence faster than expected, such that the practical limit of a measurable response is a range of 150° . This leaves a small hole ($\sim 10^\circ$ cone) in the coverage of the sensor in the direction of the spin axis, as well as around the velocity vector ($\sim 20^\circ$ cone).

5.3. Obtaining the bulk parameters from count matrices

The bulk parameters of the distribution are defined as the velocity moments of the distribution function. They have the form

$$P = \int Q(\mathbf{v}) f(\mathbf{v}) d\mathbf{v} \quad (5)$$

where $Q(\mathbf{v})$ is the moment function and the integration is taken over the whole of velocity space. The various types of moment function are listed in table 7, where \mathbf{c} is the centre-of-mass velocity.

Table 7. Moment definitions.

Parameter P	Moment function $Q(\mathbf{v})$
n density	1
\mathbf{c} bulk velocity	\mathbf{v}/n
T temperature	$(\mathbf{v} - \mathbf{c})^2 / 3kn$
\mathbf{q} heat flux vector	$mn(\mathbf{v} - \mathbf{c})^2(\mathbf{v} - \mathbf{c})/2$

Since the distribution function is measured by equation (3) at a set of discrete points distributed in velocity space, the integral in the moment equation (5) must be replaced by a summation. The measured values of the distribution function $f(\mathbf{v}_0)$ are assigned to the velocity \mathbf{v}_0 centred in the region of velocity space over which the flux was collected. In a perfectly designed instrument, the regions of velocity space in which successive measurements were made would be contiguous. In practice, this cannot be achieved. In some parts of velocity space the regions overlap; in others there are gaps between measurements. Thus

we have to divide velocity space into a set of boxes with walls halfway between neighbouring points in the set v_0 , and assume that the distribution function value is uniform across the box and equal to the value at the centre. The box is not identical with the region in which the measurement is made, but there is a considerable part common to both volumes. Then

$$p = \sum_i f(v_i) q_i$$

where

$$q_i = \int Q(v) dv.$$

In this summation the integral of the moment function $Q(v)$ is taken over the i th box to obtain q_i . It could be approximated by the value of $Q(v)$ at the centre point, multiplied by the volume of the box. However, this approximation is unnecessary and can introduce errors in the values of the coefficients used in the summation when the boxes are not small enough. For example, the coefficient for the x component of the bulk velocity is

$$[(\theta_2 - \theta_1) - \cos(\theta_2 + \theta_1) \sin(\theta_2 - \theta_1)](\sin \varphi_2 - \sin \varphi_1)(v_2^4 - v_1^4)/4$$

where $\theta_1, \theta_2, \varphi_1, \varphi_2, v_1$ and v_2 are the boundaries of the box.

Although algorithms are easily written to produce bulk parameters from any measured distribution, care must be exercised in their interpretation because the results can be misleading for several reasons.

(i) The summation may not cover the complete distribution. For example, an important part of the distribution may be lost in one of the gaps in coverage.

(ii) In natural plasmas, particularly in the most interesting boundary regions, more than one distribution may be present. An inspection of the original distribution matrix would show whether this was the case. Then separate integrations over the different distributions, if they are in distinct regions of velocity space, give the bulk parameters of each component.

(iii) The integrations are carried out over velocity space but the sensor is sensitive to the parameter E/q . Therefore it is necessary to identify the ion species and charge state. If it can be assumed that only one species is present, then the values are accurate. However, if there is a substantial fraction of another species, then the results lose accuracy.

(iv) The distribution may be so narrow that it only occupies one box. In this case the integration gives the density, but the accuracy of the velocity is limited by the size of the box, and only an upper limit can be obtained for the temperature.

5.4. Analysis of solar wind data

Points (ii), (iii) and (iv) above apply to measurements made by the fast ion sensor in the solar wind. There are two distributions present, protons and alpha particles, with different masses and different charge states, and each is so narrow that it only occupies a few of the angular bins (5.625° azimuthal $\times 13^\circ$ polar). Furthermore, the basic matrix, even with this coarse resolution relative to the distribution, i.e. 30 energies \times 8 azimuthal \times 5 polar angle = 1200 elements, was too big to be transmitted to Earth. It was compressed for transmission by summing over the polar angles to produce a matrix 30 \times 8 = 240 elements, and summing over azimuthal angles to produce a second matrix 30 \times 5 = 150 elements. A different approach from that described in § 5.3 was therefore required to obtain the bulk parameters of the solar wind distribution.

It was necessary to make some assumptions about the shape of the distribution. The simplest, and a reasonably accurate one, is to assume that it is a drifting maxwellian whose drift velocity is much greater than its thermal velocity, i.e.

$$u \gg (2kT/m)^{1/2}.$$

This approximation is certainly true if the angular distribution is,

as the observations show, only a few degrees wide. Then the distribution may be expressed approximately in spherical polar coordinates as

$$f(v) = \left(\frac{m}{2\pi kT} \right)^{3/2} \exp \left(-\frac{m}{2kT} [(v-u)^2 + u^2(\theta-\theta_0)^2 + u^2(\varphi-\varphi_0)^2 \sin^2 \theta_0] \right)$$

where the drift velocity is $u = (u, \theta_0, \varphi_0)$. This distribution can be integrated over θ or φ to obtain the two-dimensional distributions corresponding to the transmitted matrices:

$$f_1(v, \varphi) = \frac{m}{2\pi kT} \exp \left(-\frac{m}{2kT} [(v-u)^2 + u^2(\varphi-\varphi_0)^2 \sin^2 \theta_0] \right) \frac{\sin \theta_0}{u} \quad (6)$$

$$f_2(v, \theta) = \frac{m}{2\pi kT} \exp \left(-\frac{m}{2kT} [(v-u)^2 + u^2(\theta-\theta_0)^2] \right) \frac{1}{u \sin \theta_0}. \quad (7)$$

Integrating a second time over either of these distributions gives the distribution over speed

$$F(v) = \frac{1}{u^2} \left(\frac{m}{2\pi kT} \right)^{1/2} \exp \left(-\frac{m}{2kT} (v-u)^2 \right). \quad (8)$$

The electrostatic energy analyser separates the particles according to energy per charge, so the variable in the expression must be converted to energy V measured in eV. Putting

$$u^2 = 2qV_0/m \quad v^2 = 2qV/m$$

gives

$$F(V) = \frac{m}{2qV_0} \left(\frac{m}{2\pi kT} \right)^{1/2} \exp \left(-\frac{q}{4V_0 kT} (V-V_0)^2 \right).$$

The analysis now reduces to finding the mean, and the width of three gaussian functions, in energy, azimuth and polar angle.

There are some other considerations to take into account. First of all, there are many different species of ion in the solar wind. The most abundant, in order, are protons H^+ , alpha particles He^{2+} and sixfold-ionised oxygen O^{6+} . The peaks in the distribution corresponding to these three species appear at different energies, i.e. $V_0, 2V_0$ and $2.67V_0$. Depending on the widths of the distributions and their relative magnitude, the three peaks can be separated in the data. The alpha particle peak is usually distinct, but the density of O^{6+} is rarely high enough to register in a single observation. Once the proton temperature becomes too high, the wings of the proton distribution swamp the alpha particle peak and the alpha parameters cannot be derived.

Secondly, the proton distribution is characterised by two temperatures, parallel and perpendicular to the magnetic field. Since the direction of the magnetic field in space varies continually, the parallel and perpendicular directions do not generally line up with any particular coordinate system. Effectively this means that three different temperatures are derived from the three distribution widths. It is not possible to relate these three values to parallel or perpendicular temperatures.

Thirdly, occasionally the proton distribution exhibits marked differences from the maxwellian shape (Feldman *et al* 1973). In this situation a routine which attempts a detailed (e.g. least squares) fit to a maxwellian may well produce a misleading or erratic result.

Finally, if the highest count rate is recorded in one of the edge bins of the angular range, it is no longer possible to obtain flow direction or temperature, because a higher value might have been recorded beyond the edge.

The algorithm combines two approaches: moment-type integrations over the speed distribution, equation (8), to obtain density, drift speed and one value of temperature; and fitting to the gaussian distribution of equations (6) and (7) to obtain the direction of the flow θ , ϕ and two other values of the temperature. The moment integration obtains a density and drift speed by summing over the distribution and by finding its centroid respectively. This approach is insensitive to the shape of the distribution, should it be double-peaked for example, but agrees with the maxwellian formulation if that is the actual shape. The angular fitting assumes that the sensor accepts contiguous sections of the gaussian distribution in successive sweeps, or adjacent anodes, and forms ratios to obtain mean angle and angular spread. The scheme is robust in that it is not sensitive to the precise shape of the distribution and, as will be shown in § 5.5, produces results which are self-consistent, linear and much more accurate than would be expected from the size of the angular bins.

5.5. In-flight checks

Two tests allow us to derive some confidence in the accuracy of the results. First, the relation between the direction of the solar wind and the phase of the sensor's cycle can be changed by ground command by changing the delay between the Sun crossing of the Sun sensors and the Sun reference pulse distributed to the instruments. By changing the phase in a sequence of steps, the solar wind could effectively be moved across the field of view of the sensor. The operation was scheduled three times during the cruise phase. Only on one of these occasions was the solar wind direction steady enough to allow the results to be properly interpreted. This set of data is shown in figure 7. As the ϕ direction is changed one degree at a time, there are steps in the derived direction. The size of the steps is given in table 8. The angle before and after each step was obtained by averaging five successive values measured at 8 s intervals. The error quoted is the standard deviation of the samples. Much of the variation is caused by changes in the flow direction of the solar wind itself because the angle is changing systematically. As one of the steps was made, there was an almost simultaneous change in the solar wind which made it impossible to establish the size of the step. For the remaining steps the average is $1.04^\circ \pm 0.16^\circ$ for the protons and $1.36^\circ \pm 0.60^\circ$ for the alpha particles. This shows that the method of analysis is both accurate and linear. It is impossible to deduce from this type of analysis the absolute accuracy of directional measurements.

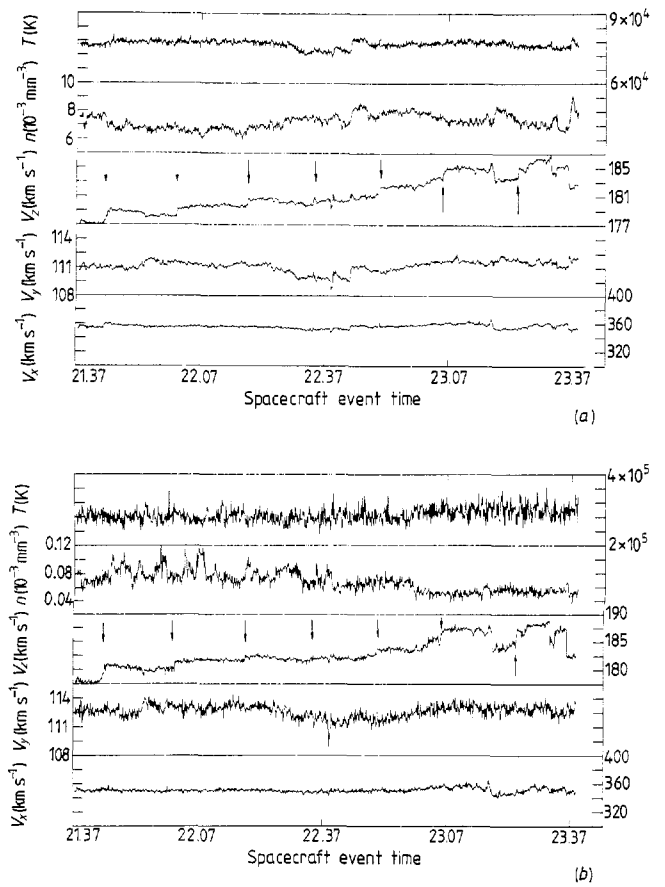


Figure 7. Solar wind (a) proton and (b) alpha parameters calculated from the transmitted matrices during the sequence of changes of the phase of the Sun reference pulse. The phase was changed by one degree at each of the arrows.

Table 8. Results from SRP scan.

Time (UT)	Proton step (deg)	Alpha particle step (deg)
21.44	1.00 ± 0.48	1.51 ± 0.90
22.01	1.02 ± 0.22	1.18 ± 0.59
22.18	0.92 ± 0.36	0.70 ± 0.45
22.34		
22.50	1.03 ± 0.39	0.84 ± 0.33
23.05	0.94 ± 0.47	1.62 ± 0.96
23.24	1.36 ± 0.24	2.33 ± 0.94
Mean	1.04 ± 0.16	1.36 ± 0.60

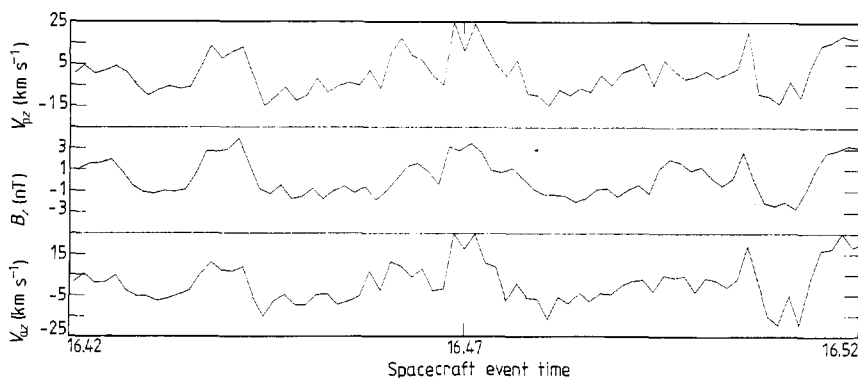


Figure 8. A sequence of Alfvén waves detected at 1.8×10^6 km from the nucleus of comet Halley. The panels, from top to bottom, show the z component of the proton velocity, the magnetic field (courtesy F Neubauer) and the alpha particle velocity.

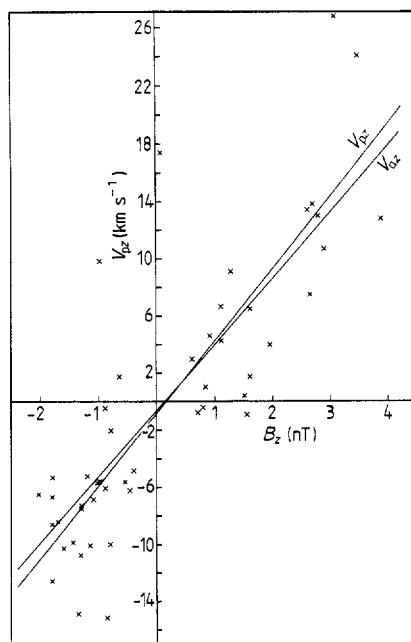


Figure 9. A scatterplot of the proton velocity z component against the magnetic field z component for the data of figure 8. The line marked V_{pz} is the result of a least squares fit to the data. The second line, V_{az} , is the result of a similar fit to the alpha particle data not shown plotted here.

The second test depends on the comparison with an independent set of data from the magnetometer.

In the region upstream from the bow shock of comet Halley, Giotto passed through a region of hydromagnetic turbulence generated by the implantation of cometary ions in the solar wind flow (Johnstone *et al* 1987). Some of the wavetrains encountered showed a clear correlation between the components of the flow velocity and the magnetic field. Such a correlation is expected for Alfvén waves for which

$$\mathbf{b} = \mathbf{v}(\mu_0 \rho)^{1/2}$$

where \mathbf{b} and \mathbf{v} are the vector disturbances in field and flow respectively. A sample of the two data sets is shown in figure 8. Figure 9 gives the results of a regression analysis of the two flow velocities and the magnetic field. The fitted lines can be expressed as

$$V_{pz} = (-1.1 + 4.8B_z) \pm 5.5 \text{ km s}^{-1}$$

$$V_{az} = (-0.9 + 4.4B_z) \pm 6.6 \text{ km s}^{-1}$$

where the error term indicates the standard deviation of points from the line. The correlation coefficients are 83% and 75% respectively. The excellence of the correlation confirms the accuracy of the analysis in obtaining the three components of the flow velocity.

6. Conclusion

The measurements obtained by the two sensors during the encounter between Giotto and comet Halley justified the original approach to the design of the instrument. It made accurate measurements of the main cometary populations over a wide range of distances from the nucleus, within the limitations imposed by the spacecraft resources.

Acknowledgments

The work at Mullard Space Science Laboratory and the Rutherford Appleton Laboratory was supported by the UK Science and Engineering Research Council. The work at the Max-Planck-Institut für Aeronomie was supported by the Max-

Planck-Gesellschaft zur Förderung der Wissenschaften and by the Bundesministerium für Forschung und Technologie under grant number 01OF112/4. The work at the Southwest Research Institute was supported by NASA contract NAS5-27442. The work at the Kiruna Geophysical Institute was supported by the Swedish Board for Space Activities. The work at the Istituto di Fisica dello Spazio Interplanetario was supported by the Piano Spaziale Nazionale of the Consiglio Nazionale delle Ricerche.

The production of this instrument required the dedicated efforts of a large number of people. In particular thanks are due to: Messrs J Raymont, A J Coker and J A Bowles at the Mullard Space Science Laboratory; H Wirbs and A Loidl at the Max-Planck-Institut für Aeronomie; R Field at Mullard Limited; J Coles and P Howarth at Cambridge Consultants Limited; E de Giorgi, P Perani and M de Bernardi at Laben; and K Rembach at Dornier System.

References

- Balsiger H, Altwegg K, Buhler F, Fischer J, Geiss J, Meier A, Rettenmund U, Rosenbauer H, Schwenn R, Benson J, Hemmerich P, Sager K, Kulzer G, Neugebauer M, Goldstein B E, Goldstein R, Shelley E G, Sanders T, Simpson D, Lazarus A J and Young D T 1986 The Giotto ion mass spectrometer
ESA SP-1077 pp 129–48
- Biermann L 1951 Kometen Schweife und solare Korpuscular strahlung
Z. Astrophys. **29** 274–86
- Biermann L, Brosowski B and Schmidt H U 1967 The interaction of the solar wind with a comet
Solar Phys. **1** 254–83
- Feldman W C, Asbridge J R, Bame S J and Montgomery M D 1973 Double ion streams in the solar wind
J. Geophys. Res. **78** 2017–27
- Ip W-H and Axford W I 1982 Theories of physical processes in cometary comae and tails
Comets ed. L L Wilkening (Tucson: University of Arizona Press) pp 588–634
- Johnstone A D, Kellock S J, Coates A J, Smith M F, Booker T and Winningham J D 1985 A space-borne plasma analyser for three-dimensional measurements of the velocity distribution
IEEE Trans. **NS-32** 139–44
- Johnstone A D, Glassmeier R H, Acuna M, Borg H, Bryant D, Coates A, Formisano V, Heath J, Mariani F, Musmann G, Neubauer F, Thomsen M, Wilken B and Winningham J 1987 Waves in the magnetic field and solar wind flow outside the bow shock at comet Halley
Astron. Astrophys. in press
- McKenna-Lawlor S, Thompson A, O'Sullivan D, Kirsh E, Melrose D and Wenzel K P 1986 The Giotto energetic particle experiment
ESA SP-1077 pp 53–65
- Rème H, Cotin F, Cros A, Medale J L, Sauvaud J A, d'Uston C, Korth A, Richter A K, Loidl A, Anderson K A, Carlson C W, Curtis D W, Lin R P and Mendis D A 1986 The Giotto RPA-Copernic plasma experiment
ESA SP-1077 pp 33–52
- Wallis M K 1973 Weakly shocked flows of the solar wind plasma through atmospheres of comets and planets
Planet. Space Sci. **21** 1647–60
- Wilken B, Weiß W, Studemann W and Hasebe N 1987 The Giotto implanted ion spectrometer (IIS): physics and technique of detection
J. Phys. E: Sci. Instrum. **20** 778–85